

## Resistive switching in graphene: A theoretical case study on the alumina-graphene interface

Renan P. Maciel<sup>1,\*</sup>, Olle Eriksson<sup>1</sup>, Yaroslav O. Kvashnin<sup>1</sup>, Danny Thonig<sup>1,2</sup>, Daria Belotckerkovtceva<sup>1</sup>, M. Venkata Kamalakara<sup>1</sup>, and Chin Shen Ong<sup>1,†</sup><sup>1</sup>Department of Physics and Astronomy, Uppsala University, Box 516, SE-75120 Uppsala, Sweden<sup>2</sup>School of Science and Technology, Örebro University, Fakultetsgatan 1, SE-70182 Örebro, Sweden

(Received 18 April 2023; accepted 6 September 2023; published 13 November 2023)

Neuromorphic computing mimics the brain's architecture to create energy-efficient devices. Reconfigurable synapses are crucial for neuromorphic computing, which can be achieved through memory-resistive (memristive) switching. Graphene-based memristors have shown nonvolatile multibit resistive switching with desirable endurance. Through first-principles calculations, we study the structural and electronic properties of graphene in contact with an ultra-thin alumina overlayer and demonstrate how one can use charge doping to exert direct control over its interfacial covalency, reversibly switching between states of conductivity and resistivity in the graphene layer. We further show that this proposed mechanism can be stabilized through the *p*-type doping of graphene, e.g., by naturally occurring defects, the passivation of dangling bonds or defect engineering.

DOI: [10.1103/PhysRevResearch.5.043147](https://doi.org/10.1103/PhysRevResearch.5.043147)

## I. INTRODUCTION

Graphene is a two-dimensional (2D) material with remarkable electronic and mechanical properties [1–5]. It is a 2D network of conjugated  $sp^2$  carbon in a hexagonal lattice along the basal plane. The  $\pi$ -cloud formed by the out-of-plane  $p_z$  orbitals above and below the basal plane of graphene is responsible for its high electron mobility, which moves like mass-less fermions. Its intrinsic carrier mobility can reach values up to  $\sim 10^5$  cm<sup>2</sup>/(V s) [6,7], making it an excellent candidate for high-speed devices. However, the  $\pi$ -cloud itself is also self-passivating and chemically inert and therefore does not typically demonstrate an affinity towards many substrates, ligands, or solvents. Coupled with the Klein tunneling phenomenon [8], there has been a long-standing difficulty in drastically and reversibly changing the conductivity of graphene as a function of the gate,  $V_G$ , and drain-to-source voltage,  $V_{DS}$ .

Recent successes in overcoming these challenges have led to the development of graphene-based memristive devices non-breaking space with [9–13] capable of resistive switching, which is being pursued for resistive random-access memory (ReRAM) devices. These devices have programmable conductance that can be changed with short, high amplitude voltage pulses [14,15], making them central to the construction of reconfigurable neuromorphic synapses

[16–18]. Since memristive devices can both compute and store data, they are much more energy-efficient than conventional microchips, consuming only a thousandth of the energy of a conventional computer processor [19]. As a result, they are widely seen as the future of computing after almost five decades of complementary metal-oxide semiconductor (CMOS) technology growth.

In 2015, Tian *et al.* [20] demonstrated that an artificial synapse based on twisted bilayer graphene and alumina could exhibit dynamic tunable plasticity. More recently, Schranghamer *et al.* [21] constructed a multibit nonvolatile graphene-based memristor that was capable of switching between high and low conductance states. In the latter, the authors found that interactions at the alumina|graphene interface dominated the memristive mechanisms, rather than the bulk of the alumina substrate. Graphene was *p*-doped and OH ligands bound to the Al sites of the alumina substrate during device fabrication. The conductance states were programmed into the device via pulses of  $V_{DS}$ , and the resistance was modulated by varying  $V_G$ . Unlike traditional oxide-based memristors (which are driven by the formation and degradation of conductive filaments in the oxide), the switching mechanism of the graphene-based resistive memory device was distinct and dominated by interactions at the alumina|graphene interface.

In addition to Refs. [20,21], many other experiments non-breaking space with [22–27] have also investigated the interfacial properties of the alumina|graphene system. Alumina is widely used in graphene electronics and spintronics as a gate dielectric and as tunnel barrier [22,24] owing to its large experimental bandgap of 5.0–8.8 eV [28,29]. A theoretical understanding of the alumina|graphene interface is crucial for optimizing experimental techniques to enhance the performance of graphene-based devices. However, theoretical works usually only study the isolated properties of alumina separate from the graphene system [30–34] due to computational cost

\*renan.maciell@physics.uu.se

†chinshen.ong@physics.uu.se

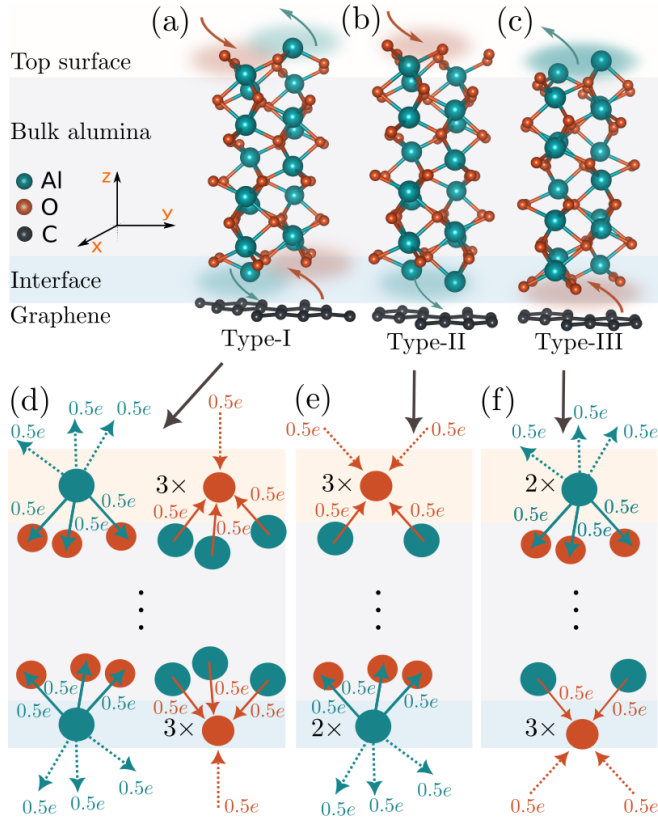


FIG. 1. Schematic illustrations of the unrelaxed slab supercell for a perfectly stoichiometric ultra-thin alumina overlayer,  $\text{Al}_2\text{O}_3$ , as deposited on top of graphene in the (a) type-I, (b) type-II, and (c) type-III configurations. The green and orange shaded regions highlight the unsaturated Al and O bonds, respectively, at the top alumina surface. The outward (inward) direction of the arrows indicates the tendency of the unsaturated Al (O) to donate (accept) electrons. Bond analyses for the surface and interface terminations of the alumina are depicted in (d)–(f) for the type-I, -II, and -III configurations, respectively.

and only limited theoretical analyses of how alumina interacts with graphene [35] have been reported.

In the present work, we study the structural and electronic properties of alumina of the  $\alpha\text{-Al}_2\text{O}_3$  polymorph (i.e., corundum), as an ultra-thin overlayer in contact with graphene and how different contact conditions at the interface between alumina and graphene can produce significantly varied conductive/resistive properties.

Traditionally [36], the mechanisms for memristive switching include capacitive gating [37], phase transitions [38,39], ion-defect migration [40–42], filament formation [43,44], and interfacial reactions [45–47]. In graphene-based memristors, voltage-controlled charge traps in lateral or vertical structures, e.g., via the tuning of VG or the introduction of interfacial traps [20,21,48–50], have also been used.

Through first-principles calculations, we propose a non-volatile memristive switching mechanism that can controllably and reversibly alternate between a conductive and resistive state of graphene. Our proposed mechanism does not involve the bulk of the alumina substrate and clearly explains why *p*-doped graphene is conductive. It also shows how

dissociative OH-adsorption may, in fact, facilitate memristive switching, which is in excellent agreement with the experimental observation of Ref. [21]. We further show that under the right conditions, the switching mechanism may even turn on and off magnetic moments at the interface, as has also been experimentally observed [51].

## II. PERFECT STOICHIOMETRY: THE $\text{Al}_2\text{O}_3$ GRAPHENE INTERFACE

We first constructed a supercell consisting of a stoichiometric slab of a 1.3-nm alumina layer on top of graphene [Figs. 1(a)–1(c)], based on experimental data [51]. The alumina layer has perfect stoichiometry, and all bonds within the bulk of alumina are coordinated, except at the top surface and bottom contact interface (Fig. 1). This also implies that any *p*- or *n*-type doping in the system can only be caused by unsaturated Al and/or O at the surface and interface, not bulk defects in alumina. Since the alumina layer may have different surface and interface terminations, we identify three representative types of geometric configurations and label them as types I, II, and III. Figures 1(a)–1(c) show the unrelaxed supercells of these configurations. In stoichiometric alumina, each  $\text{Al}^{3+}$  is coordinated to six  $\text{O}^{2-}$  while each  $\text{O}^{2-}$  is coordinated to four  $\text{Al}^{3+}$ . It can be concluded that for each Al-O ionic bond,  $\text{Al}^{3+}$  donates  $3e/6 = 0.5e$  to the bond (where  $e$  is the electron charge), whereas  $\text{O}^{2-}$  accepts  $2e/4 = 0.5e$  from the bond. In other words, Al is an *electron donor*, while O is an *electron acceptor*. For more information on the model, see Appendix A. In this section, we focus our discussion on the alumina/graphene interface, although the same analysis can be applied to the top surface of alumina.

The alumina type-I configuration has unsaturated Al and O at the contact interface. Specifically, this supercell has one unsaturated Al (with three dangling bonds) and three unsaturated O (with one dangling bond each) at the interface. Bond analysis shows that the three dangling O bonds require ( $3 \times 0.5e =$ ) 1.5 electrons to fully occupy the O shells, while the three dangling Al bonds need to donate 1.5 electrons to empty the Al shells. Therefore the three dangling Al bonds donate 1.5 electrons to the three dangling O bonds, resulting in autocompensation of charge transfer [30] and complete charge neutrality of alumina at the interface. Relaxation of the atomic positions of the structure through density functional theory (DFT) force minimization reveals that the unsaturated Al interacts mainly with the unsaturated O in its immediate vicinity to form a coplanar bond that avoids interacting strongly with the graphene layer underneath. These coplanar bonds (at the interface and surface) are shaded in gray in Fig. 2(a). As a result, only weak van der Waals interaction exists between alumina and graphene, as reflected through the relatively large separation of  $\sim 0.293$  nm, and the presence of the alumina layer does not substantially change the graphene electronic band structure. (See Appendix B for more details related to the DFT calculations.) The relaxed type-I configuration also has the lowest calculated total energy of the three relaxed configuration types. (See Table I for a summary of the energies of the different configurations). Unlike the type-I configuration, the type-II configuration only has unsaturated Al at the contact interface [Fig. 1(e)]. Without unsaturated O

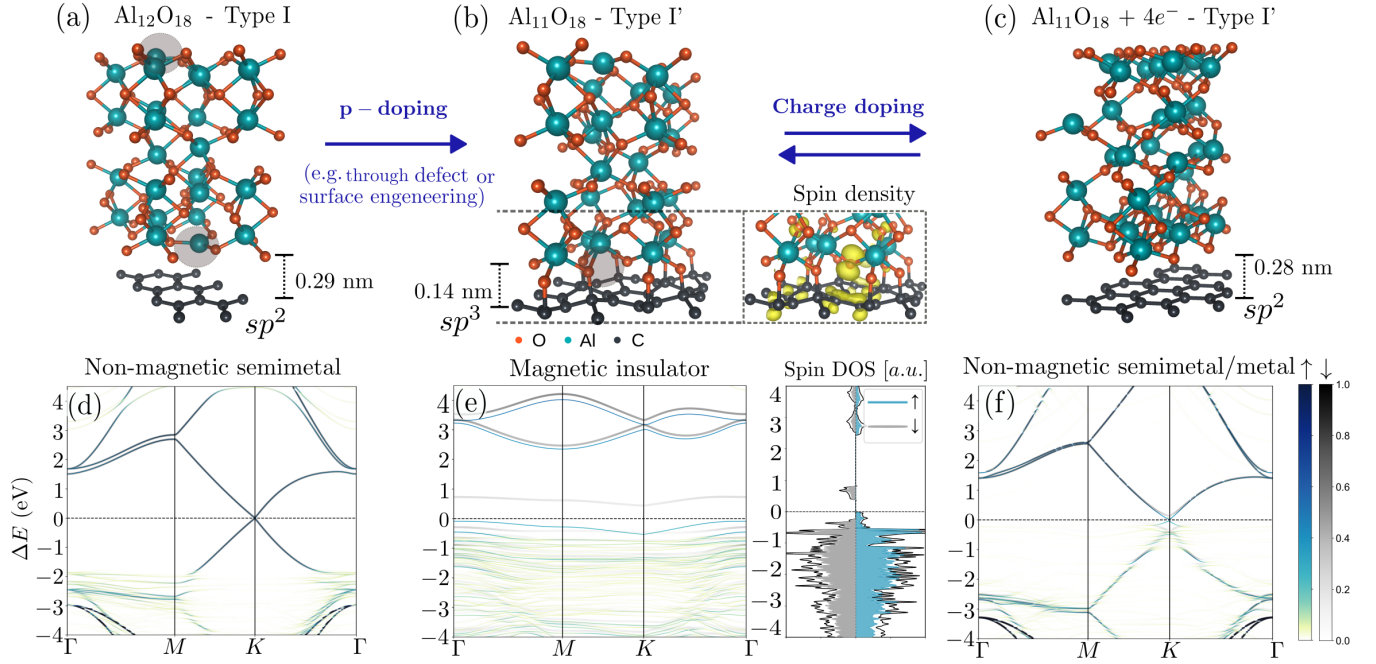


FIG. 2. (a) Perfectly stoichiometric alumina as deposited on graphene in the type-I configuration after relaxation. The gray-shaded region highlights the co-planar bonds that are formed due to auto-compensation between the unsaturated Al and O at the surface and interface. (b) Al-vacancy-stabilized type-I' configuration (i.e., Al<sub>11</sub>O<sub>18</sub>). The gray-shaded region shows that with the removal of Al, co-planar bond formation is no longer favored. The C-O bond at the interface is 0.14-nm long, indicating the activation of interfacial covalency. (c) The  $sp^3$  graphene bonds can be reverted back to  $sp^2$  graphene bonds with charge doping. The C-O bond at the interface is destroyed and the alumina-graphene separation of 0.29 nm is restored. (d)–(f) show the spin-polarized band structures of (a)–(c), respectively, projected onto the pseudo-wave-functions of graphene. The degrees of spin-up and spin-down projections are represented using color bars. (e, inset) shows the spin-projected density of state of (b) and its inset shows the spin densities plot in yellow.

acting as electron acceptors for electrons originating from the unsaturated Al, the tendency for the unsaturated Al to donate electrons at the interface leads to strong repulsive potential energy from graphene  $\pi$ -cloud, making the unrelaxed structure of the type-II configuration highly unstable and will not be further discussed.

On the other hand, the type-III configuration only has unsaturated O at the interface [Fig. 1(f)]. Interestingly, unlike the type-I configuration, the type-III configuration does not form any co-planar bonds after relaxation. Instead, the electron-accepting unsaturated O at the interface prefers to interact with the graphene  $\pi$ -cloud to induce  $sp^3$  hybrid states in graphene that cause out-of-plane deformations of the graphene sheet [see Appendix C, Fig. 5(a)]. The resultant C-O covalent bonds are  $\sim 0.148$ -nm long, which is half the alumina-graphene van-der-Waals separation in the type-I con-

figuration. The formation of covalent  $sp^3$  graphene bonds at the interface (i.e., interfacial covalency) dramatically distorts the electronic structure of graphene, disrupting the  $\pi$ -cloud and destroying even the Dirac cone to form a bandgap of  $\sim 2.33$  eV [see Appendix C, Fig. 5(b)], i.e., these  $sp^3$  bonds are resistive. We found that the relaxed type-III configuration (which has  $sp^3$  graphene bonds) is less stable than the relaxed type-I configuration (which has  $sp^2$  graphene bonds), with the latter being  $\Delta E_t = 9.33$  eV lower in total energy per supercell (Table I). Here,  $E_t$  denotes the calculated total energy of the system, whereas  $\Delta E_t$  denotes its difference with respect to the configuration type that has the lowest  $E_t$ .

Summarizing, an important conclusion can be made: the presence of electron acceptors (such as unsaturated O) at the interface can activate an interaction with the graphene  $\pi$ -cloud. If the interaction is strong enough, the  $sp^2$  hybridization of graphene can be distorted to form  $sp^3$  bonds.

### III. STABILIZING THE RESISTIVE STATE OF GRAPHENE

Even though the formation of  $sp^3$  graphene bonds is higher in energy than the formation of  $sp^2$  graphene bonds when the perfectly stoichiometric alumina overlayer is deposited on top of it, slightly off-stoichiometric alumina layers can arise naturally during the fabrication process or be achieved through defect engineering, stabilizing these  $sp^3$  bonds. We will study these stabilizing mechanisms in this section.

TABLE I. Summary of the energy and magnetic properties of the Al<sub>12</sub>O<sub>18</sub>/graphene slab, where  $E_t$  denotes the calculated total energy of the system, and  $\Delta E_t$  denotes its difference with respect to the configuration type that has the lowest  $E_t$ .

Al <sub>12</sub> O <sub>18</sub> /graphene	Type I	Type II	Type III
$\Delta E_t$ per supercell (eV)	0.00	—	9.33
$\mu_B$ per supercell	0.00	—	1.17
$\mu_B$ of unsaturated O atom	0.00	—	0.32



TABLE II. Summary of the energy and magnetic properties of the  $\text{Al}_{11}\text{O}_{18}$ |graphene interface, where  $E_t$  and  $\Delta E_t$  are defined as in Table I.

$\text{Al}_{11}\text{O}_{18}$  graphene	Type I'	Type II'	Type III'
$\Delta E_t$ per supercell (eV)	0.00	2.86	—
$\mu_B$ per supercell	1.00	2.79	—
$\mu_B$ of unsaturated O atom	0.47	0.75	—

### A. Defect formations in alumina

First, we focus on the effects of fabricating the device in a natural (O-rich) ambient atmosphere, which favors the formation of Al vacancies over O vacancies in alumina, resulting in the off-stoichiometric form of  $\text{Al}_{11}\text{O}_{18}$ . The off-stoichiometric form of  $\text{Al}_{12}\text{O}_{17}$ , which may be fabricated in an O-deficient atmosphere, is discussed in the Appendix E. We keep the labels of the original configurations and additionally use a single prime (') to denote the  $\text{Al}_{11}\text{O}_{18}$  stoichiometry (i.e., types I' and II'). The original type-I, -II, and -III configurations have one [Fig. 1(d)], two [Fig. 1(e)], and zero [Fig. 1(f)] unsaturated Al at the interface per supercell, respectively. Due to the geometries, our investigation is restricted to type-I' and -II' configurations only (Appendix D, Fig. 6). We note that since O is an electron acceptor and Al is an electron donor, off-stoichiometric  $\text{Al}_{11}\text{O}_{18}$  and  $\text{Al}_{12}\text{O}_{17}$  are vacancy-induced  $p$ - and  $n$ -doped, respectively.

Removing one unsaturated Al from the type-I interface [Figs. 1(a), 1(d) and 2(a)] forms the type-I' interface [Fig. 2(b)], leading to the creation of three more unsaturated O. This makes the type-I' interface similar to the type-III interface [Fig. 1(c)], except that it has a higher concentration of unsaturated O. Like the type-III interface, the  $sp^3$  graphene bond is preferentially formed upon force minimization in the calculations, also resulting in a similar bandgap of 2.1 eV [Fig. 2(e)]. Unlike the type-III interface, however, which is the less stable on-stoichiometric structure (Table I), the type-I' interface is the more stable off-stoichiometric structure (Table II and Appendix D for details about the type-II' interface). This is remarkable, as it verifies that the  $sp^3$  graphene bonds can, in fact, be stabilized through the Al-vacancy-induced  $p$ -type doping of alumina. Not only did the vacancy-induced  $p$ -type doping increase the electron affinity of alumina, the increased concentration of electron-accepting unsaturated O at the interface also strengthened its interaction with the graphene  $\pi$ -cloud. Finally, we then repeat our analysis for  $n$ -doped alumina as induced by O vacancy, i.e.,  $\text{Al}_{12}\text{O}_{17}$ . Under no conditions are  $sp^3$  bonding formed in graphene after relaxation (see Appendix E).

### B. Passivation of dangling bonds in alumina

In realistic devices, dangling bonds (such as those at the surface, interface and defects) are naturally passivated by atoms and ligands. Motivated by the experiments of Ref. [21], we will discuss in this section how dissociative OH-adsorption of  $\text{H}_2\text{O}$  at the (top) alumina surface [as shown in Figs. 8(a) and 8(b)] may also stabilize the  $sp^3$  graphene bonds. In principle, the contact interface [21] can also be passivated with the same outcome, but will not be discussed in this work for con-

ciseness. Due to the geometries, we will only investigate the passivation of type-III  $\text{Al}_{12}\text{O}_{18}$  by OH (Fig. 8, Appendix F). Since hydroxide (OH) is an electron acceptor, OH-adsorption will induce  $p$ -type doping. (The  $n$ -type doping via passivation by electron-donating H is also studied and will be discussed in Appendix G).

We found that when the dangling surface bonds of type-III  $\text{Al}_{12}\text{O}_{18}$  are passivated with OH, the  $sp^3$  graphene bonds continue to persist in the OH-passivated type-III configuration. Moreover, OH-passivation stabilizes the formation of  $sp^3$  graphene bonds: without passivation, only two out of three unsaturated O per supercell are bonded to graphene via the  $sp^3$  bonds; upon passivation, all three unsaturated O are bonded to graphene via the  $sp^3$  bonds. The calculated DFT band structure for the OH-passivated type-III configuration is similarly gapped with a bandgap of  $\sim 1.27$  eV for spin down channel and  $\sim 1.41$  eV for the spin up channel. The main consequence of OH-passivation is that the buckling of graphene becomes more extensive. In the memristive device of Ref. [21], it was found that the dissociative OH-adsorption of  $\text{H}_2\text{O}$  that happens during the graphene transfer process of device fabrication is inevitable and Ref. [52] suggests that it may even persist further through surface passivation, leading to the distinct  $p$ -type doping of the device. Our calculations lend support as to why a  $p$ -type environment is conducive for graphene-based memristive switching observed in experiment [21]. We repeat our calculation to study the  $n$ -type doping of H-passivation for the type-II configuration. H-passivation does not lead to any  $sp^3$  graphene bonds being formed (see Appendix G).

Finally, we note here that the charge transfer between alumina and graphene  $\pi$ -cloud is dominated by the surface termination of alumina at the interface (i.e., proximity effects) and not the vacancy-induced doping of bulk alumina. As long as alumina is O-terminated at the interface,  $p$ -type doping of graphene is observed, independent of whether bulk alumina is  $p$ - or  $n$ -doped either through (Al or O) vacancy formation or the (OH or H) passivation of dangling bonds (Figs. 6 and 7).

### C. Switching between the resistive and conductive state

Even though the  $\pi$ -electrons of a pristine layer of  $sp^2$ -bonded graphene are both highly mobile and chemically resistant, when an alumina overlayer is deposited on top of it and is naturally  $p$ -doped, the resistive but otherwise unstable  $sp^3$  bonds (Sec. II) in graphene are stabilized (Secs. III A and III B). This suggests that charge doping may be used to switch between the resistive  $sp^3$  state and the conductive  $sp^2$  state and vice versa. Charge doping may be stimulated through the application of high-amplitude voltages via a gold contact [as we propose in Fig. 3(a)] or the application of  $V_{\text{DS}}$  (as experimentally reported in Ref. [21]) or  $V_{\text{G}}$  pulses.

To investigate theoretically if electron doping can revert a resistive  $sp^3$  state to a conductive  $sp^2$  state, we inject electrons into the relaxed vacancy-stabilized ( $2 \times 2$ )-supercell of type-I with only one Al vacancy (i.e.,  $\text{Al}_{47}\text{O}_{72}$ , which has 1/4 the vacancy concentration of type I') and found that even though the concentration of  $sp^3$  bonds is also reduced by a factor 1/4 compared to type I', the band structure of the system remains gapped. Furthermore, only  $0.5e$  (not  $4e$ , as it is for type I') per

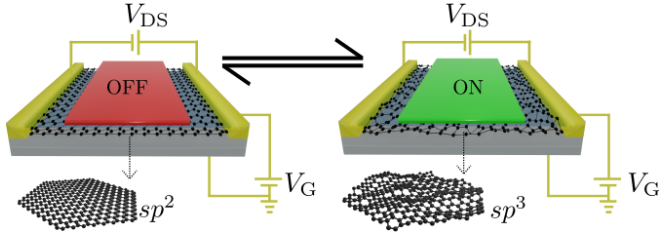


FIG. 3. The proposed design of graphene memristor. The red and green plates, respectively, represent gold contacts that can be used to activate the resistive and conductive graphene states, via the application of voltage pulse. The alumina overlayer, sandwiched between graphene and the gold contacts, are made semitransparent in this figure for illustration only. Here,  $V_{DS}$  denotes drain-to-source voltage, while  $V_G$  denotes gate voltage.

$(1 \times 1)$ -supercell is then needed to fully restore the  $sp^2$  bonds in graphene and its conductive state. Similarly, if 100% of all the unsaturated O at the type-III surface are passivated with OH [i.e., three per  $(1 \times 1)$ -supercell],  $4e$  per  $(1 \times 1)$ -supercell is needed to revert the resistive  $sp^3$  bonds to conductive  $sp^2$  bonds [Figs. 8(b) and 8(d)]. A lower concentration of OH adsorption requires a lower concentration of electrons to revert the  $sp^3$  bonds to  $sp^2$  bonds, similar to the effects of lowering of Al-vacancy concentration.

Moreover, our calculations show that dangling bonds from unsaturated O form localized O impurity states at the Fermi level that are spin-polarized, in agreement with experiment [51]. The unsaturated O bonds leads to spin polarization, as is clear from Figs. 2(b) and 2(e). The unsaturated O at the interface also polarizes the C atoms of the graphene layer and the atoms in its immediate surroundings. These states are responsible for generating the spontaneous local magnetic moment and are particularly interesting because they may explain, for example, the reduced spin lifetime in graphene observed in spintronics experiments [53]. See Appendix H for further discussion related to spin polarization.

#### IV. CONCLUSION

The work presented here suggests that  $sp^3$  bonds can serve as reversible carrier traps that are resistive synaptic junctions for resistive switching, as an alternative to voltage-controlled charge traps [20,49,50]. We hope that this work will inspire transformative changes for memristor-based neural networks, which aim to radically improve the performance of digital circuits without shrinking transistors, circumventing Moore's law while overcoming the obstacles related to energy consumption that are currently impeding the more widespread adoption of artificial intelligence (AI) methods.

#### ACKNOWLEDGMENTS

R.P.M. is grateful to Ivan P. Miranda for fruitful discussions. The computational resources for this work were enabled by resources provided by the Swedish National Infrastructure for Computing (SNIC), partially funded by the Swedish Research Council. The authors also acknowledge European Research Council (ERC) (synergy grant FASTCORR, project No. 854843 Consolidator Grant SPINNER, Project No. 10

1002772), the Kunt and Alice Wallenberg foundation (KAW), the Swedish Energy Agency (Energimyndigheten), StandUPP, and eSSENCE. Y.O.K. acknowledges the financial support from the Swedish Research Council (VR) under Project No. 2019-03569 and the Göran Gustafsson Foundation. D.T. acknowledges the financial support from the Swedish Research Council (VR) under Project No. 2019-03666

#### APPENDIX A: THE MODEL

##### 1. The slab construction

###### a. Perfect stoichiometry: $\text{Al}_{12}\text{O}_{18}$

We first constructed a supercell consisting of a stoichiometric slab of  $(1 \times 1)$  (0001)-terminated alumina unit cell on top of a  $(2 \times 2)$  graphene supercell [Figs. 1(a)–1(c)]. The thickness of the alumina layer was approximately 0.13 nm, based on experimental data [51]. The  $(2 \times 2)$ -supercell of graphene has a hexagonal lattice and in-plane supercell lattice vectors of  $|\mathbf{a}_1| = |\mathbf{a}_2| = 0.492$  nm, while alumina has a hexagonal unit cell and in-plane unit-cell lattice vectors of  $|\mathbf{b}_1| = |\mathbf{b}_2| = 0.476$  nm. The lattice mismatch with respect to the graphene supercell is 3.25%. Due to this mismatch, a small strain must be applied to the graphene and/or alumina in order to construct a commensurate slab of reasonable size. We have chosen to strain the oxide instead of compressing graphene to ensure that the most relevant electronic properties of graphene are preserved, and the only influence is due to the interaction with alumina in a slightly compressed state. We will further show in Sec. A2 that the main conclusions of this work are not affected by straining either graphene or alumina in the calculations. Particular attention was paid to the choice of the initial distance between graphene and the oxide layer before structural relaxation was performed, since this choice may enhance or diminish the chemical interaction at the interface, leading to different (meta)stable solutions depending on this initial choice. For this reason, we set this distance to an initial value of  $\sim 0.2$  nm for all models studied in this work before structural relaxation. This distance was chosen based on the convergence of the energy minima after considering different initial distances within a range of 0.1 to 0.35 nm.

Since the alumina layer may have different surface terminations and form different contact interfaces with graphene, we identify three representative types of geometric configurations and label them as types I, II, and III. These three distinct

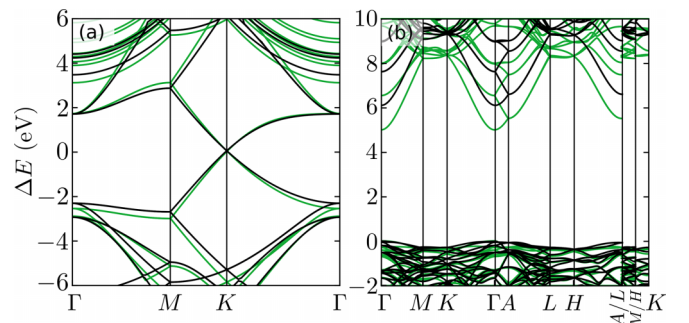


FIG. 4. Superposition of the unstrained (black) and strained (green) band structure for (a) graphene monolayer with compression of  $\sim 3.25\%$ , and for (b) strained hexagonal bulk  $\text{Al}_{12}\text{O}_{18}$ .

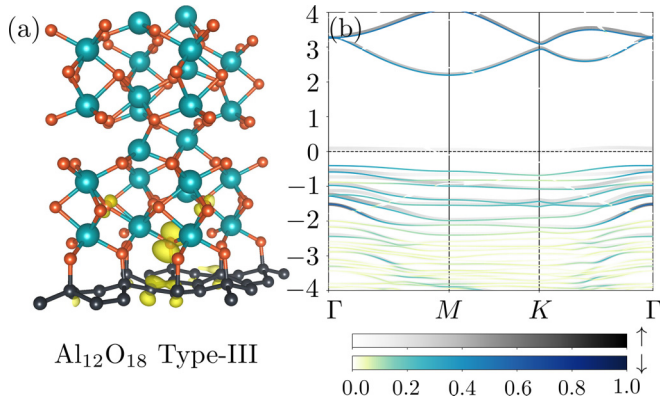


FIG. 5. (a) Type-III configuration after relaxation. (b) Spin-polarized band structure projected onto the pseudo-wave-functions of graphene.

configurations are related by the shift of the (0001)-plane of the hexagonal unit cell of alumina in the [0001]-direction (i.e., the  $z$ -direction). Figures 1(a)–1(c) show the unrelaxed supercells of these configurations, with the dangling bonds at the surface and interface shaded in green and orange for unsaturated Al and O, respectively.

#### b. Off-Stoichiometry: $\text{Al}_{11}\text{O}_{18}$

For each stoichiometry, we started from the three types of unrelaxed stoichiometric configurations (Fig. 1) as introduced

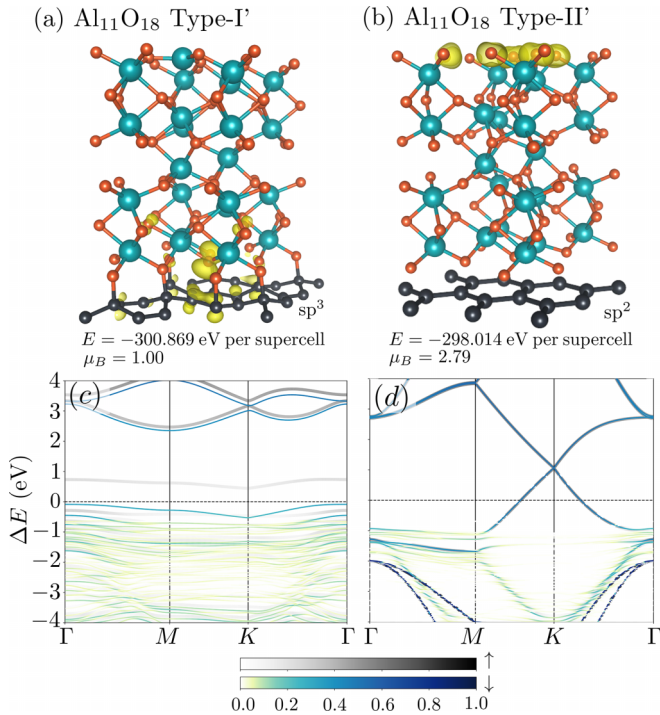


FIG. 6.  $\text{Al}_{11}\text{O}_{18}$  as deposited on graphene (a) type-I' and (b) -II' configuration after relaxation. Here,  $E$  refers to the total energy per supercell and  $\mu_B$  the magnetization in Bohr magnetons. (c-d) The band structure of graphene in the presence of  $\text{Al}_{11}\text{O}_{18}$ . (d) shows that when oxygen is near graphene, graphene becomes  $p$ -doped through proximity effects, even though there are no  $sp^3$  bonds formed in graphene. The isosurfaces of the spin densities are plotted in yellow.

in Sec. II and removed an unsaturated Al from the interface while keeping the surface of the alumina layer intact. We then performed force minimization to obtain the relaxed structure. Since the type-III configuration only has unsaturated O at the interface and no unsaturated Al [Fig. 1(f)], our investigation of Al vacancies in the  $\text{Al}_{11}\text{O}_{18}$  stoichiometry was restricted to only the type-I' and -II' configurations.

## 2. Strained versus unstrained system

We first studied the effects of strain on the band structures of bulk alumina (under tensile strain) and the  $(2 \times 2)$  graphene supercell (under compressive strain). Here, we exchanged the lattice parameters of both lattices so that strained alumina had an in-plane unit-cell lattice constant of 0.492 nm, while strained graphene has an in-plane supercell lattice constant of 0.476 nm. Using the constrained lattice parameters, we relaxed all atomic positions of both systems through force minimization. After relaxation, the in-plane C-C bond length of graphene decreased from 0.142 to 0.137 nm, whereas the Al-O bonds for alumina increased from 1.86 and 1.97 nm to 1.91 and 2.01 nm, respectively. The calculated band structures of graphene and bulk alumina are shown in Figs. 4(a) and 4(b), respectively. For graphene, the applied compression of the supercell is not enough to change its band structure significantly. The reduction of approximately  $\sim 3\%$  of C-C bond length is insufficient to distort the linear dispersion at the Fermi level. Moreover, since the applied strain does not violate either the time-reversal or space inversion symmetry, which protects the presence of Dirac cone, the system remains gapless, as expected [4,54]. However, the increased overlap between bonding and anti-bonding states, as shown in Fig. 4(a). For alumina, the increase in Al-O bond length induces a bandgap reduction from  $\sim 6.12$  eV to  $\sim 5.00$  eV, as shown in Fig. 4(b). From this analysis, we conclude that a study of the electronic structure of the  $\text{Al}_{12}\text{O}_{18}$ |graphene system with a common in-plane lattice constant can be done either by adapting the lattice constant to alumina or vice versa without changing our main conclusions. In this work, we have chosen to construct the  $\text{Al}_{12}\text{O}_{18}$ |graphene interface by adapting the in-plane lattice constant of the oxide layer to that of graphene.

## APPENDIX B: COMPUTATIONAL DETAILS

Our theoretical investigation was modeled after the experimental configurations of our recent publication [51], as well as device structures of experimental significance, e.g., tunnel junctions, memristors, and graphene spintronics devices, as mentioned above. We note that even though Ref. [51] was published by the same research team behind this work, the former contains primarily experimental findings focused on the experimental stabilization of magnetic moments at the interface, while this work discusses theoretical results focused on identifying a memristive switching mechanism in graphene.

All density functional theory (DFT) calculations were performed using the Vienna *ab initio* simulation package (VASP) [55–57] using the projector augmented wave method with Perdew-Burke-Ernzerhof (PAW-PBE) exchange-correlation functionals [58]. van der Waals interactions between the oxide and graphene were incorporated using the Becke-Jonson



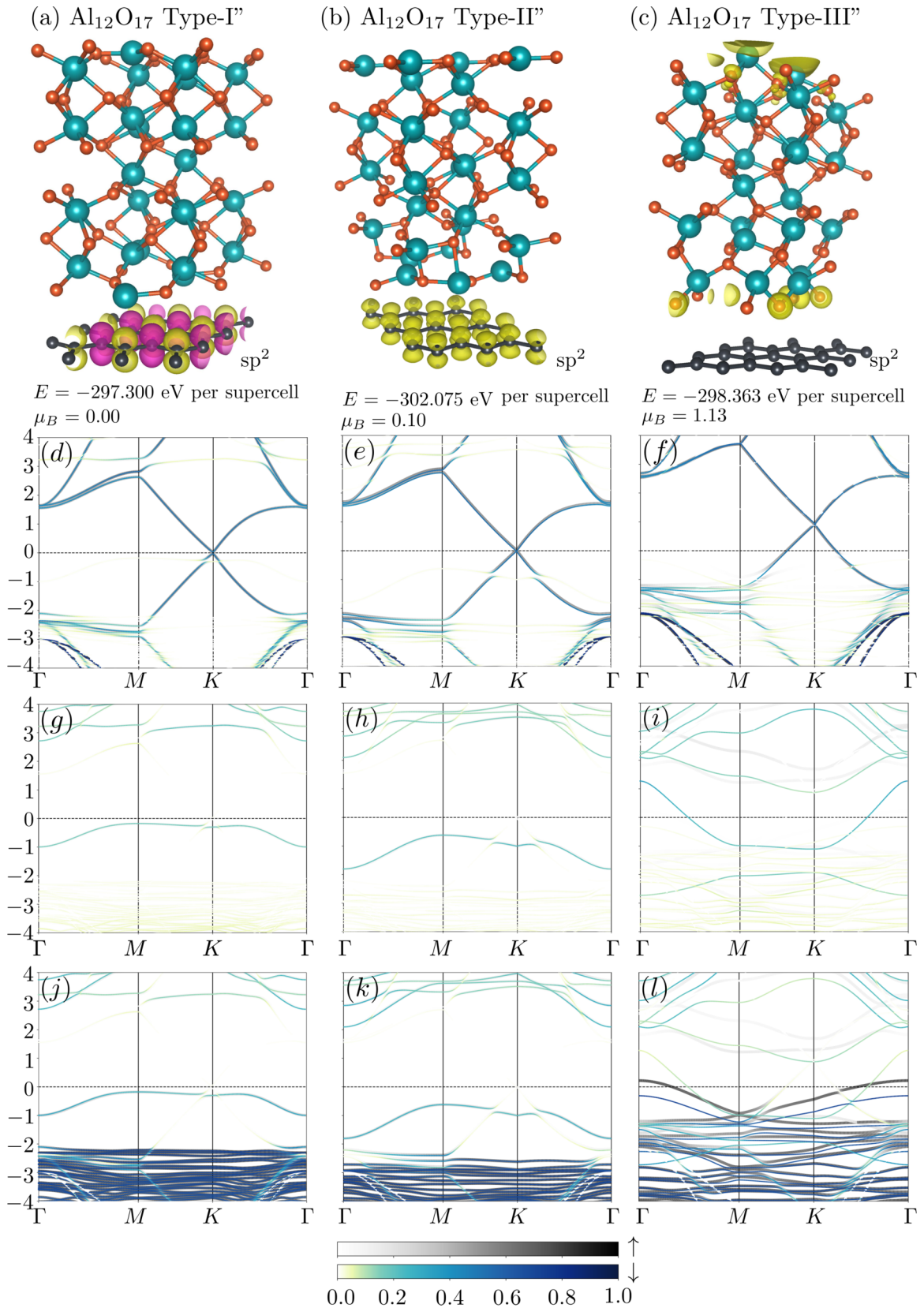


FIG. 7.  $\text{Al}_{12}\text{O}_{17}$  as deposited on graphene (a) type-I', (b) -II', and (c) -III' configurations after relaxation. Here,  $E$  refer to the total energy per supercell and  $\mu_B$  the magnetization in Bohr magnetons. (e)–(m) show the spin-polarized band structure projected onto the pseudo-wave-functions of different atoms: (e)–(g), (h)–(j), and (k)–(m) show the band structures when projected onto the C, Al, and O orbitals, respectively. (c) and (g) show that when the alumina layer is O-terminated at the interface, graphene becomes  $p$ -doped through proximity effects, even though there are no  $\text{sp}^3$  bonds formed in graphene. The spin-up and spin-down isosurfaces of the spin densities are plotted in yellow and pink, respectively.

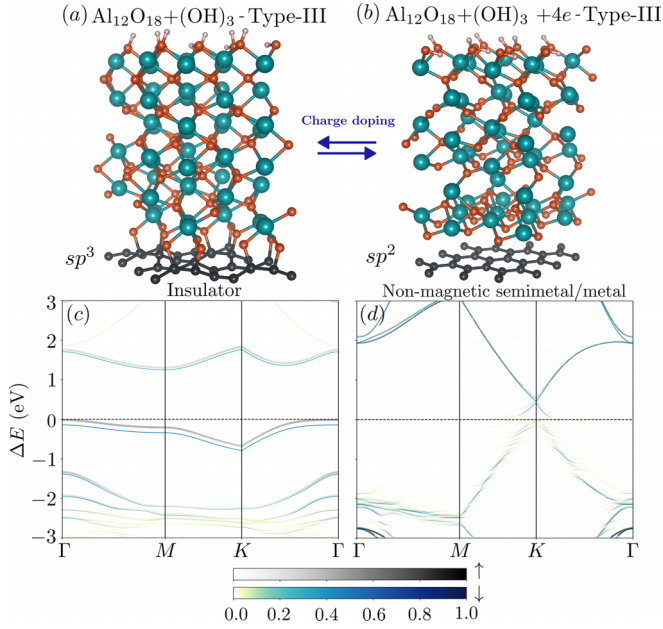


FIG. 8. (a) Perfectly stoichiometric alumina of type-III configuration as deposited on graphene after OH-passivation, which stabilizes the  $sp^3$  graphene bonds at the interface. Pink sphere represents the H of the OH ligands. (b) The  $sp^3$  graphene bonds can be reverted back to  $sp^2$  graphene bonds with charge doping. (c) and (d) show that the spin-polarized band structures of (a) and (b), respectively, projected onto the pseudo-wave-functions of graphene. The degrees of spin-up and spin-down projections are represented using color bars. The Fermi level of (c) has been shifted up by  $\sim 0.268$  eV to the top of the valence bands.

damping method [59,60]. The kinetic-energy cutoff for the plane-wave expansion of the wave functions was set to 520 eV and the Kohn-Sham equations were evaluated on a  $\mathbf{k}$ -grid of  $6 \times 6 \times 1$ . Dipole correction was made to remove the spurious interactions between the slab and its periodic images. Geometric relaxation, which was performed by minimizing every force component on the ions to less than  $10^{-4}$  eV/nm, excluded effects due to spin polarization.

#### APPENDIX C: THE $\text{Al}_{12}\text{O}_{18}$ |GRAPHENE INTERFACE: TYPE III

The type-III configuration only has unsaturated O at the interface and does not form any co-planar bonds after relaxation [Figs. 1(f) and 5(a)]. The electron-accepting unsaturated O at the interface interacts with the graphene  $\pi$ -cloud to induce  $sp^3$  hybrid states in graphene that cause out-of-plane deformations of the graphene sheet. The formation of covalent  $sp^3$  graphene bonds at the interface (i.e., interfacial covalency) dramatically distorts the electronic structure of graphene, disrupting the  $\pi$ -cloud and destroying even the Dirac cone to form a bandgap of  $\sim 2.33$  eV [Fig. 5(b)], i.e., these  $sp^3$  bonds are resistive.

#### APPENDIX D: THE $\text{Al}_{11}\text{O}_{18}$ |GRAPHENE INTERFACE: TYPE II'

The removal of one unsaturated Al from the type-II interface leaves behind one unsaturated Al and three unsaturated

TABLE III. Summary of the energy and magnetic properties of the  $\text{Al}_{12}\text{O}_{17}$ |graphene interface

$\text{Al}_{12}\text{O}_{17}$  graphene	Type I''	Type II''	Type III''
$\Delta E_t$ per supercell (eV)	4.77	0.00	3.71
$\mu_B$ per supercell	0.00	0.10	0.25
$\mu_B$ of unbonded O atom	0.00	0.00	0.00

O per supercell at the type-II' interface. Upon relaxation,  $sp^2$  bonding in graphene is still preferred over  $sp^3$  bonding. Moreover, the type-II' interface is  $\Delta E_t = 2.846$  eV per supercell higher in energy than the type-I' interface. We conclude that even though autocompensation is now possible for the type-II' interface, it still cannot stabilize the  $p$ -type doping of alumina induced by the Al vacancy defect as effectively as the disruption of the graphene  $\pi$ -cloud and the concomitant formation of  $sp^3$  bonding can. The relevant information about  $\text{Al}_{11}\text{O}_{18}$ |graphene interface is shown in Fig. 6.

#### APPENDIX E: THE $\text{Al}_{12}\text{O}_{17}$ |GRAPHENE INTERFACE: TYPES I'', II'', AND III''

The O removal causes charge imbalance in the newly constructed geometries compared to the stoichiometric cases. Since all O at the interface have similar coordination numbers, this removal is done randomly. After relaxation, the lack of oxygen forces the ultra thin alumina film to reconstruct next to the graphene layer [see reconstructed interface in Fig. 7(b)]. Unlike  $\text{Al}_{12}\text{O}_{18}$ |graphene cases, all  $\text{Al}_{12}\text{O}_{17}$ |graphene structures avoid covalent bond formation between the oxygen of the slab and graphene. This suggests that any interaction between the oxide and graphene occurs via van der Waals forces once there is an oxygen deficiency. The final distance between graphene and the oxide for all  $\text{Al}_{12}\text{O}_{17}$ |graphene geometries increases to  $\sim 0.3$  nm. In terms of stability, we found that the most stable structure is the type-II'' configuration.

From the electronic structure perspective, the most stable geometry (i.e., type-II'' configuration) does not show any significant change in the graphene band structure. However, the absence of O forces Al to partially hybridize with the  $\pi$ -orbital of graphene. This hybridization does not shift or open a gap of the graphene Dirac cone, as it is shown in Fig. 7(f) (which is similar to the type-I'' geometry). Instead, it mainly modifies the valence bands below the Fermi level [see Figs. 7(i) and 7(l)]. In contrast, for a less stable geometry [i.e., type-III'', Fig. 7(c)], O interacts indirectly with the graphene layer via charge transfer between O and C atoms without any  $sp^3$  or covalent bond formation that would cause structural distortion of graphene. Therefore the Dirac cone shifts  $\sim 1.2$  eV above the Fermi level, indicating significant  $p$ -type doping, as shown in Fig. 7(g).

#### APPENDIX F: HYDROXIDE SURFACE TERMINATION: TYPE III

When passivating dangling bonds, we ensured that the attached atom or ligand correctly fills the electron shell; otherwise, artificial doping may occur due to excess or lack of electrons in the overall system. This restricts the number of configuration types that can be studied. Specifically, since



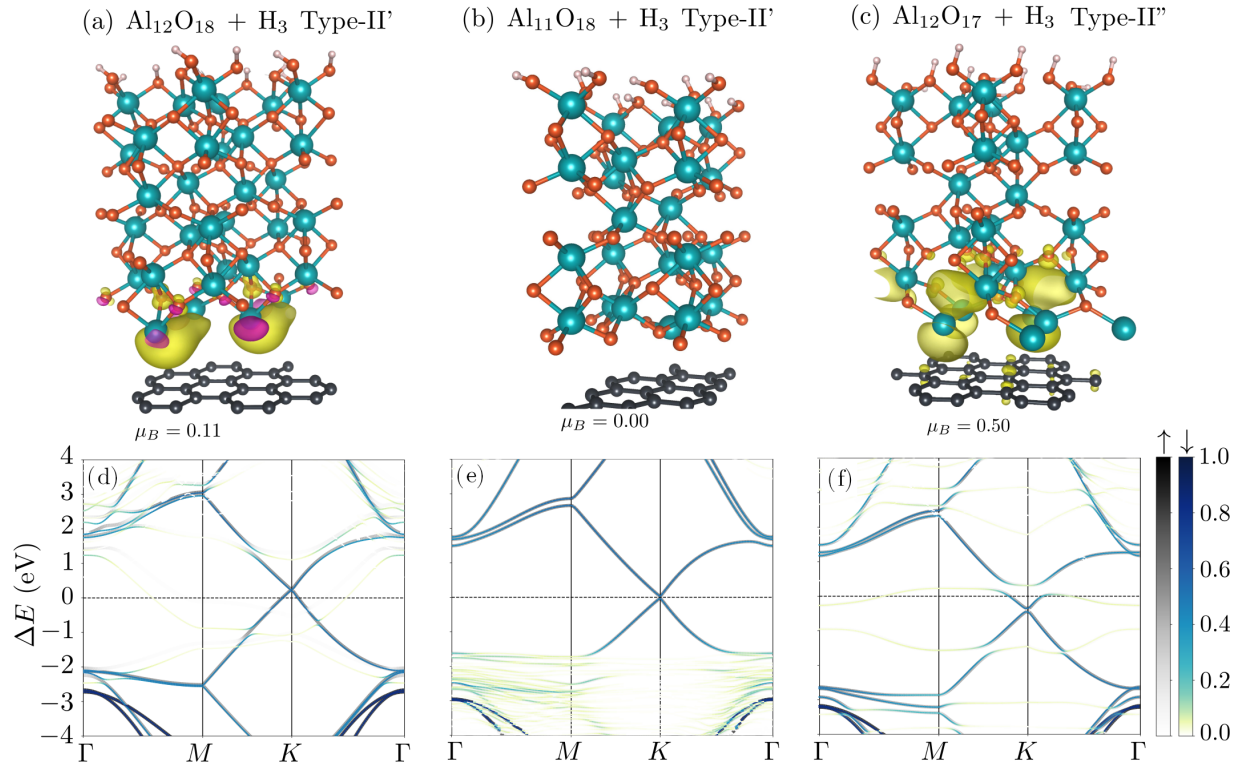


FIG. 9. H-passivated alumina for all the type-II configurations, namely, types II, II', and II''. (a)–(c) show the  $\text{Al}_{12}\text{O}_{18}$ ,  $\text{Al}_{11}\text{O}_{18}$ , and  $\text{Al}_{12}\text{O}_{17}$  systems that have, respectively, been H-passivated. The spin-up and spin-down isosurfaces of the spin densities are plotted in yellow and pink, respectively. Here,  $\mu_B$  denotes magnetization in Bohr magnetons. [(d)–(f)] Spin-polarized band structures projected onto the pseudo-wavefunctions of graphene orbitals for (a)–(c), respectively.

the type-I surface of  $\text{Al}_{12}\text{O}_{18}$  is already auto-compensated [Figs. 1(a) and 1(b)], no passivation is needed. The type-II surface of  $\text{Al}_{12}\text{O}_{18}$  contains only electron-accepting unsaturated O [Figs. 1(b) and 1(e)] and should only be passivated by H, not OH. Since the type-III surface of  $\text{Al}_{12}\text{O}_{18}$  is unique in containing only unsaturated Al that are uncompensated [Figs. 1(c) and 1(f)], we will only investigate the passivation of type-III  $\text{Al}_{12}\text{O}_{18}$  by OH (Fig. 8). Starting from the unrelaxed type-III configuration, we attach an OH ligand to every unsaturated O at the surface [Figs. 1(c) and 1(f)] and relax the structure through force minimization.

#### APPENDIX G: HYDROGEN SURFACE TERMINATION: TYPES-II, -II' AND -II''

We use hydrogen to saturate dangling O bonds to form hydroxide ligands for the stoichiometric and off-stoichiometric of types II, II', II'' and allow full relaxation to obtain the final structure, such that there are no dangling O bonds at the top surface. Since the alumina/graphene interface is not saturated, it is expected that the graphene  $\pi$ -cloud can still be affected by alumina. For instance, the band structure of  $\text{Al}_{12}\text{O}_{18} + 3\text{H}$  type II, i.e., the Fermi level is shifted below the Dirac point [Fig. 9(a)]. In addition, Al/O states hybridize with the  $\pi$ -cloud and induce graphene to be metallic. Unlike  $\text{Al}_{12}\text{O}_{18} + 3\text{H}$  type II and  $\text{Al}_{12}\text{O}_{17} + 3\text{H}$  type II', the Al deficiency of  $\text{Al}_{11}\text{O}_{18} + 3\text{H}$  type II' has no substantial effects on the  $\pi$ -orbital of carbon atoms [Fig. 9(b)]. In the absence of electron-accepting O,  $\text{Al}_{12}\text{O}_{17} + 3\text{H}$  type II'', electrons

originating from the Al atom causing the Fermi level to be raised relative to the Dirac cone, i.e., *n*-type doping [Fig. 9(c)]. In all cases, however, when alumina is saturated with hydrogen at the top surface, no  $sp^3$  bonds are formed at the interface with graphene.

#### APPENDIX H: SPIN POLARIZATION EFFECTS

All the DFT band structure calculations presented here are spin-polarized. For some of the configurations, the slab construction of the alumina layer imposes unsaturated, dangling bonds and uncompensated charges at the top alumina surface and contact interface, such that spontaneous spin polarization may be expected. Unlike unsaturated O, perfectly coordinated O with filled chemical bonds are closed-shell where all electrons are paired, leading to no spin polarization. In the presence of unsaturated O, our calculations show that dangling bonds from unsaturated O form localized O impurity states at the Fermi level that are spin-polarized, as also observed in experiment [51]. As a result, spin polarization tends to emerge when there is unsaturated O at the contact interface (e.g., in type-III  $\text{Al}_{12}\text{O}_{18}$  and type-I'  $\text{Al}_{11}\text{O}_{18}$ ) or the top alumina surface (e.g., in type-II'  $\text{Al}_{11}\text{O}_{18}$ ). Furthermore, the presence of unsaturated O is more probable when there are Al vacancies (e.g., the  $\text{Al}_{11}\text{O}_{18}$  off-stoichiometry) than there are O vacancies (e.g., all  $\text{Al}_{11}\text{O}_{18}$  configurations are all nonmagnetic). In Tables I–III, we summarize the calculated local magnetic moment for all configurations.

In Fig. 2(e), we show the spin-projected density of states of the type-I'  $\text{Al}_{11}\text{O}_{18}$  configuration (inset) and its spin-polarized band structure projected onto the pseudo-wave-functions of graphene. Our calculations show that dangling bonds from unsaturated O form localized O impurity states at the Fermi level that are spin-polarized, as was also observed in experiment [51]. As a result, the band structure in Fig. 2(e) exhibits the spin-up (blue) and spin-down (red) exchange splitting, of which only the spin-down states are found above the Fermi level. Unlike perfectly coordinated O, which are closed-shell (i.e., all electrons are paired), unsaturated O leads to spin polarization. Figure 2(b,right) shows an isosurface of the spin

density at the interface. The unsaturated O at the interface polarizes the C atoms of the graphene layer and the atoms in its immediate surroundings. These states are responsible for generating the spontaneous magnetization found in the unsaturated oxygen atoms and are interesting because they may explain, for example, the reduced spin lifetime in graphene observed in spintronics experiments [53]. We found that the local magnetic moment (at the top surface) due to the unsaturated O will also vanish if passivated (e.g., by OH or H). This raises the interesting question of how magnetization at the surface and interface of the oxide may be stabilized, but remains outside the scope of this work.

- 
- [1] A. K. Geim and K. S. Novoselov, The rise of graphene, *Nat. Mater.* **6**, 183 (2007).
  - [2] M. I. Katsnelson, Graphene: Carbon in two dimensions, *Mater. Today* **10**, 20 (2007).
  - [3] J. McClure, Diamagnetism of graphite, *Phys. Rev.* **104**, 666 (1956).
  - [4] A. H. Castro Neto, F. Guinea, N. M. R. Peres, K. S. Novoselov, and A. K. Geim, The electronic properties of graphene, *Rev. Mod. Phys.* **81**, 109 (2009).
  - [5] P. R. Wallace, The band theory of graphite, *Phys. Rev.* **71**, 622 (1947).
  - [6] K. I. Bolotin, K. J. Sikes, Z. Jiang, M. Klima, G. Fudenberg, J. Hone, P. Kim, and H. Stormer, Ultrahigh electron mobility in suspended graphene, *Solid State Commun.* **146**, 351 (2008).
  - [7] S. Morozov, K. Novoselov, M. Katsnelson, F. Schedin, D. C. Elias, J. A. Jaszczak, and A. Geim, Giant intrinsic carrier mobilities in graphene and its bilayer, *Phys. Rev. Lett.* **100**, 016602 (2008).
  - [8] M. I. Katsnelson, K. S. Novoselov, and A. K. Geim, Chiral tunnelling and the Klein paradox in graphene, *Nat. Phys.* **2**, 620 (2006).
  - [9] Y.-J. Huang and S.-C. Lee, Graphene/h-BN heterostructures for vertical architecture of RRAM design, *Sci. Rep.* **7**, 9679 (2017).
  - [10] Y. Li, A. Sinitskii, and J. M. Tour, Electronic two-terminal bistable graphitic memories, *Nat. Mater.* **7**, 966 (2008)–971.
  - [11] B. Standley, W. Bao, H. Zhang, J. Bruck, C. N. Lau, and M. Bockrath, Graphene-based atomic-scale switches, *Nano Lett.* **8**, 3345 (2008).
  - [12] Q. A. Vu, H. Kim, V. L. Nguyen, U. Y. Won, S. Adhikari, K. Kim, Y. H. Lee, and W. J. Yu, A high-on/off-ratio floating-gate memristor array on a flexible substrate via CVD-grown large-area 2D layer stacking, *Adv. Mater.* **29**, 1703363 (2017).
  - [13] X. Wang, W. Xie, and J. B. Xu, Graphene based non-volatile memory devices, *Adv. Mater.* **26**, 5496 (2014).
  - [14] F. M. Bayat, M. Prezioso, B. Chakrabarti, H. Nili, I. Kataeva, and D. Strukov, Implementation of multilayer perceptron network with highly uniform passive memristive crossbar circuits, *Nat. Commun.* **9**, 2331 (2018).
  - [15] M. Hu, C. E. Graves, C. Li, Y. Li, N. Ge, E. Montgomery, N. Davila, H. Jiang, R. S. Williams, J. J. Yang, Q. Xia, and J. P. Strachan, Memristor-based analog computation and neural network classification with a dot product engine, *Adv. Mater.* **30**, 1705914 (2018).
  - [16] D. Marković, A. Mizrahi, D. Querlioz, and J. Grollier, Physics for neuromorphic computing, *Nat. Rev. Phys.* **2**, 499 (2020).
  - [17] A. Rao, P. Plank, A. Wild, and W. Maass, A long short-term memory for AI applications in spike-based neuromorphic hardware, *Nat. Mach. Intell.* **4**, 467 (2022).
  - [18] W. Wang, L. Danial, Y. Li, E. Herbelin, E. Pikhay, Y. Roizin, B. Hoffer, Z. Wang, and S. Kvatinsky, A memristive deep belief neural network based on silicon synapses, *Nat. Electron.* **5**, 870 (2022).
  - [19] K.-E. Harabi, T. Hirtzlin, C. Turck, E. Vianello, R. Laurent, J. Droulez, P. Bessière, J.-M. Portal, M. Bocquet, and D. Querlioz, A memristor-based Bayesian machine, *Nat. Electron.* **6**, 52 (2022).
  - [20] H. Tian, W. Mi, X.-F. Wang, H. Zhao, Q.-Y. Xie, C. Li, Y.-X. Li, Y. Yang, and T.-L. Ren, Graphene dynamic synapse with modulatable plasticity, *Nano Lett.* **15**, 8013 (2015).
  - [21] T. F. Schranghamer, A. Oberoi, and S. Das, Graphene memristive synapses for high precision neuromorphic computing, *Nat. Commun.* **11**, 5474 (2020).
  - [22] W. Amamou, Z. Lin, J. van Baren, S. Turkyilmaz, J. Shi, and R. K. Kawakami, Contact induced spin relaxation in graphene spin valves with  $\text{Al}_2\text{O}_3$  and MgO tunnel barriers, *APL Mater.* **4**, 032503 (2016).
  - [23] B. Fallahzad, K. Lee, G. Lian, S. Kim, C. M. Corbet, D. A. Ferrer, L. Colombo, and E. Tutuc, Scaling of  $\text{Al}_2\text{O}_3$  dielectric for graphene field-effect transistors, *Appl. Phys. Lett.* **100**, 093112 (2012).
  - [24] Y. Feng, D. J. Trainer, and K. Chen, Graphene tunnel junctions with aluminum oxide barrier, *J. Appl. Phys.* **120**, 164505 (2016).
  - [25] M. Z. Iqbal, S. Siddique, and A. Rehman, Enhanced intervalley scattering of aluminum oxide-deposited graphene, *Carbon* **124**, 188 (2017).
  - [26] Z. Li, G. Fan, Z. Tan, Q. Guo, D. Xiong, Y. Su, Z. Li, and D. Zhang, Uniform dispersion of graphene oxide in aluminum powder by direct electrostatic adsorption for fabrication of graphene/aluminum composites, *Nanotechnology* **25**, 325601 (2014).
  - [27] Y. Tateno, F. Mitsushashi, M. Adachi, T. Yonemura, Y. Saito, Y. Yamamoto, and T. Nakabayashi, An investigation to determine the interface condition between graphene and aluminum oxide, *Jpn. J. Appl. Phys.* **59**, 124001 (2020).

- [28] R. Bharthasaradhi, and L. Nehru, Structural and phase transition of  $\alpha$ - $\text{Al}_2\text{O}_3$  powders obtained by Co-precipitation method, *Phase Transitions* **89**, 77 (2016).
- [29] E. O. Filatova and A. S. Konashuk, Interpretation of the changing the band gap of  $\text{Al}_2\text{O}_3$  depending on its crystalline form: connection with different local symmetries, *J. Phys. Chem. C* **119**, 20755 (2015).
- [30] J. Ahn and J. Rabalais, Composition and structure of the  $\text{Al}_2\text{O}_3$  {0001}-(1  $\times$  1) surface, *Surf. Sci.* **388**, 121 (1997).
- [31] M. Causa, R. Dovesi, C. Pisani, and C. Roetti, *Ab initio* characterization of the (0001) and (1010) crystal faces of  $\alpha$ -alumina, *Surf. Sci.* **215**, 259 (1989).
- [32] T. French and G. A. Somorjai, Composition and surface structure of the (0001) face of  $\alpha$ -alumina by low-energy electron diffraction, *J. Phys. Chem.* **74**, 2489 (1970).
- [33] T. Godin and J. P. LaFemina, Atomic and electronic structure of the Corundum ( $\alpha$ -alumina) (0001) surface, *Phys. Rev. B* **49**, 7691 (1994).
- [34] V. Puchin, J. Gale, A. Shluger, E. Kotomin, J. Günster, M. Brause, and V. Kempter, Atomic and electronic structure of the corundum (0001) surface: Comparison with surface spectroscopies, *Surf. Sci.* **370**, 190 (1997).
- [35] T. T. Song, M. Yang, J. W. Chai, M. Callsen, J. Zhou, T. Yang, Z. Zhang, J. S. Pan, D. Z. Chi, Y. P. Feng *et al.*, The stability of aluminium oxide monolayer and its interface with two-dimensional materials, *Sci. Rep.* **6**, 1 (2016).
- [36] J. Zhu, T. Zhang, Y. Yang, and R. Huang, A comprehensive review on emerging artificial neuromorphic devices, *Appl. Phys. Rev.* **7**, 011312 (2020).
- [37] M. Ziegler, M. Oberländer, D. Schroeder, W. H. Krautschneider, and H. Kohlstedt, Memristive operation mode of floating gate transistors: A two-terminal MemFlash-cell, *Appl. Phys. Lett.* **101**, 263504 (2012).
- [38] T. Driscoll, H.-T. Kim, B.-G. Chae, M. Di Ventra, and D. N. Basov, Phase-transition driven memristive system, *Appl. Phys. Lett.* **95**, 043503 (2009).
- [39] A. Rana, C. Li, G. Koster, and H. Hilgenkamp, Resistive switching studies in  $\text{VO}_2$  thin films, *Sci. Rep.* **10**, 3293 (2020).
- [40] C. Gu and J.-S. Lee, Flexible hybrid organic-inorganic Perovskite memory, *ACS Nano* **10**, 5413 (2016).
- [41] B. Hwang, C. Gu, D. Lee, and J.-S. Lee, Effect of halide-mixing on the switching behaviors of organic-inorganic hybrid perovskite memory, *Sci. Rep.* **7**, 43794 (2017).
- [42] E. J. Yoo, M. Lyu, J.-H. Yun, C. J. Kang, Y. J. Choi, and L. Wang, Resistive switching behavior in organic-inorganic hybrid  $\text{CH}_3\text{NH}_3\text{Pb}_{1-x}\text{Cl}_x$  perovskite for resistive random access memory devices, *Adv. Mater.* **27**, 6170 (2015).
- [43] W. Sun, B. Gao, M. Chi, Q. Xia, J. J. Yang, H. Qian, and H. Wu, Understanding memristive switching via in situ characterization and device modeling, *Nat. Commun.* **10**, 3453 (2019).
- [44] Y. Zhang, G.-Q. Mao, X. Zhao, Y. Li, M. Zhang, Z. Wu, W. Wu, H. Sun, Y. Guo, L. Wang, X. Zhang, Q. Liu, H. Lv, K.-H. Xue, G. Xu, X. Miao, S. Long, and M. Liu, Evolution of the conductive filament system in  $\text{HfO}_2$ -based memristors observed by direct atomic-scale imaging, *Nat. Commun.* **12**, 7232 (2021).
- [45] K. Baek, S. Park, J. Park, Y.-M. Kim, H. Hwang, and S. H. Oh, *In situ* TEM observation on the interface-type resistive switching by electrochemical Redox reactions at a  $\text{TiN}/\text{PCMO}$  interface, *Nanoscale* **9**, 582 (2017).
- [46] I. Kim, M. Siddik, J. Shin, K. P. Biju, S. Jung, and H. Hwang, Low temperature solution-processed graphene oxide/ $\text{Pr}_{0.7}\text{Ca}_{0.3}\text{MnO}_3$  based resistive-memory device, *Appl. Phys. Lett.* **99**, 042101 (2011).
- [47] V. K. Sangwan, D. Jariwala, I. S. Kim, K.-S. Chen, T. J. Marks, L. J. Lauhon, and M. C. Hersam, Gate-tunable memristive phenomena mediated by grain boundaries in single-layer  $\text{MoS}_2$ , *Nat. Nanotechnol.* **10**, 403 (2015).
- [48] M. Park, S. Park, and K.-H. Yoo, Multilevel nonvolatile memristive and memcapacitive switching in stacked graphene sheets, *ACS Appl. Mater. Interfaces* **8**, 14046 (2016).
- [49] H. Wang, Y. Wu, C. Cong, J. Shang, and T. Yu, Hysteresis of electronic transport in graphene transistors, *ACS Nano* **4**, 7221 (2010).
- [50] G. Zebrev, E. Melnik, and A. Tselykovskiy, Interface traps in graphene field effect devices: Extraction methods and influence on characteristics, *arXiv:1405.5766*.
- [51] D. Belotckerkovtceva, R. P. Maciel, E. Berggren, R. Maddu, T. Sarkar, Y. O. Kvashnin, D. Thonig, A. Lindblad, O. Eriksson, and M. V. Kamalakar, Insights and implications of intricate surface charge transfer and  $\text{sp}^3$ -defects in graphene/metal oxide interfaces, *ACS Appl. Mater. Interfaces* **14**, 36209 (2022).
- [52] W. Kim, A. Javey, O. Vermesh, Q. Wang, Y. Li, and H. Dai, Hysteresis caused by water molecules in carbon nanotube field-effect transistors, *Nano Lett.* **3**, 193 (2003).
- [53] N. Tombros, C. Jozsa, M. Popinciuc, H. T. Jonkman, and B. J. Van Wees, Electronic spin transport and spin precession in single graphene layers at room temperature, *Nature (London)* **448**, 571 (2007).
- [54] S. Sahu and G. Rout, Band gap opening in graphene: a short theoretical study, *Int. Nano Lett.* **7**, 81 (2017).
- [55] G. Kresse and J. Furthmüller, Efficiency of *ab-initio* total energy calculations for metals and semiconductors using a plane-wave basis set, *Comput. Mater. Sci.* **6**, 15 (1996).
- [56] G. Kresse and J. Furthmüller, Efficient iterative schemes for *ab initio* total-energy calculations using a plane-wave basis set, *Phys. Rev. B* **54**, 11169 (1996).
- [57] G. Kresse and J. Hafner, *Ab initio* molecular dynamics for liquid metals, *Phys. Rev. B* **47**, 558 (1993).
- [58] G. Kresse and D. Joubert, From ultrasoft pseudopotentials to the projector augmented-wave method, *Phys. Rev. B* **59**, 1758 (1999).
- [59] S. Grimme, S. Ehrlich, and L. Goerigk, Effect of the damping function in dispersion corrected density functional theory, *J. Comput. Chem.* **32**, 1456 (2011).
- [60] H. Schröder, A. Creon, and T. Schwabe, Reformulation of the D3(Becke-Johnson) dispersion correction without resorting to higher than  $C_6$  dispersion coefficients, *J. Chem. Theory Comput.* **11**, 3163 (2015).